

EQUILIBRIUM AND FLUX SURFACE ISSUES IN THE DESIGN OF NCSX

A. REIMAN,^{*a} S. HIRSHMAN,^b S. HUDSON,^a D. MONTICELLO,^a P. RUTHERFORD,^a
A. BOOZER,^c A. BROOKS,^a R. HATCHER,^a L. KU,^a E. A. LAZARUS,^d H. NEILSON,^a
D. STRICKLER,^b R. WHITE,^a and M. ZARNSTORFF^a

^aPrinceton Plasma Physics Laboratory, P.O. Box 451, Princeton, New Jersey 08543

^bOak Ridge National Laboratory, P.O. Box 2009, Oak Ridge, Tennessee 37831

^cColumbia University, New York, New York 10027

^dGeneral Atomics, P.O. Box 85608, San Diego, California 92186-5608

Received October 17, 2005

Accepted for Publication January 13, 2006

Equilibrium issues encountered in the design of the National Compact Stellarator Experiment (NCSX) are discussed, focusing particularly on equilibrium magnetic islands. Significant improvements have been made to the VMEC equilibrium code to deal with numerical challenges at the low aspect ratios characterizing the NCSX design. Modifications to the PIES code have increased its speed, allowing routine evaluation of flux surfaces for candidate configurations. An optimizer has been built around the PIES code for healing magnetic islands, modifying the coil shapes to suppress resonant components of the magnetic field while preserving desired physics and engineering properties. The modified coils produce improved flux surface quality for a range of configurations. Neoclassical effects, which are not included in the PIES calculations, are estimated using a cylindrical model and are found to further reduce island widths significantly.

KEYWORDS: stellarator, MHD, equilibrium

I. INTRODUCTION

As the aspect ratio of stellarators decreases, the strength of the three-dimensional (3-D) geometric coupling effects increases, and the computational difficulty of magnetohydrodynamic (MHD) equilibrium calculations increases correspondingly, as does the tendency to lose flux surfaces. This paper discusses equilibrium issues encountered in the design of the National Compact

Stellarator Experiment (NCSX), focusing particularly on the issues of magnetic island formation and healing of magnetic islands.

The VMEC equilibrium code has been used for the routine generation of 3-D equilibria for stability and transport studies for NCSX, and it has been incorporated in an optimizer for generating candidate NCSX configurations and assessing coil set flexibility. VMEC uses a magnetic field representation that assumes good flux surfaces, and flux surface issues have been addressed using the PIES code. An optimizer has been built around the PIES code for modifying coil designs to produce magnetic fields with good flux surfaces while preserving other desired physics properties of the plasma configuration, and preserving desired engineering properties of the coils. Improvements have been made to both the VMEC and PIES codes in response to the needs of the NCSX study.

The VMEC code and VMEC code improvements are described in Sec. II. Section III describes the PIES code and PIES code improvements. Section IV discusses the evaluation of flux surfaces for candidate configurations generated by the optimizer. Flux surfaces are destroyed by resonant fields, and Section V describes how the resonant fields in PIES are calculated using quadratic flux-minimizing surfaces. Once calculated, the resonant fields can be eliminated. Section VI describes a method that has been used to make small modifications to the fixed-boundary NCSX configuration to remove residual magnetic islands. This procedure is adapted to free-boundary equilibria, and Sec. VII describes a procedure based on the PIES code to modify the coil design to remove resonant Fourier components generated by the discrete coils that cause flux surface breakup. This procedure is called island healing, and the coil set thus obtained is called the (M45h) healed coil set. Section VIII describes several calculations with the healed coils whose purpose is to determine the robustness of the healing effect: results

*E-mail: reiman@pppl.gov

from multifilament (as opposed to single-filament) healed coil set calculations used to model the finite thickness of the coils, various vacuum configurations with the healed coils, and an equilibrium at $\beta = 4.6\%$ comparing the healed coils to the unhealed coils.

The calculations described in Secs. IV through VIII do not include neoclassical effects, which are expected to reduce island widths. The expected consequences of neoclassical effects are estimated in Sec. IX.

II. THE VMEC CODE

The VMEC code¹ solves the 3-D equilibrium equations using a representation for the magnetic field that assumes nested flux surfaces. VMEC uses an inverse moments method, in which the geometric coordinates R and Z are expanded in Fourier series in a poloidal angle and the (geometric) toroidal angle (for nonaxisymmetric configurations). The coefficients R_{mn} , Z_{mn} in this series are functions of the normalized toroidal flux s , where $s = 0$ at the magnetic axis (which can be a helical curve in three dimensions) and $s = 1$ at the plasma boundary. Here, m is the poloidal and n is the toroidal Fourier mode number. The Fourier coefficients $R_{mn}(s = 1)$ and $Z_{mn}(s = 1)$ at the boundary can either be constants (corresponding to a “fixed-boundary” equilibrium), or they may be self-consistently computed from the MHD force balance equation at the plasma-vacuum interface (for a “free-boundary” calculation²).

Internally, VMEC computes an additional “renormalization” stream function λ , which is used to optimize, dynamically and at every radial surface, the convergence rate in Fourier space for the spectral sum $\Sigma(R_{mn}^2 + Z_{mn}^2)$. In the original (pre-2000 version) of VMEC, the radial mesh grid was staggered, with the $R_{mn}(s)$ and $Z_{mn}(s)$ coefficients defined on integral radial mesh points $s_j = (j - 1)/(N_s - 1)$, where N_s is the number of radial surfaces, and the lambda coefficients on (half-integral) mesh points interleaving the s_j mesh. For large aspect ratio plasmas, this scheme leads to excellent radial resolution as well as minimal mesh separation (with angular meshes of limited resolution).

Significant improvements have been made to the VMEC code to deal with numerical challenges at the low aspect ratios characterizing the NCSX design. VMEC2000 (the updated version of VMEC used in this work) has been redifferenced to improve the convergence both on finer angular and radial meshes and for equilibria with a wide range of rotational transform profiles. In VMEC2000, the inverse equations are cast as second-order equations (in minor radius) for the Fourier components of R , Z , and λ . As noted above, λ was previously differenced on a radial mesh centered between R , Z nodes, which greatly improved the radial resolution. This could be done to second-order accuracy (in $h_s = 1/[N_s - 1]$) since no

radial derivatives of λ appear in the determining equation, $J^s = 0$. (Here, J^s is the contravariant radial component of the current, which vanishes in equilibrium.) Near the magnetic axis, however, a type of numerical interchange instability (mesh separation) has been observed as the angular resolution was refined. This behavior previously prevented the temporal convergence of 3-D solutions with large numbers of poloidal (m) and toroidal (n) modes (typically, $m \sim 6$ to 8 was the practical limitation). Convergence problems were also observed for equilibria with low ι ($\ll 1$), where field lines must encircle the magnetic axis many times to define magnetic surfaces. The new differencing scheme encoded in VMEC2000 computes the stream function on the same radial mesh as R and Z (although the values of λ continue to be output on the centered grid for backward compatibility), which leads to numerical stabilization of the numerical origin interchange instability. To avoid first-order errors (in h_s) near the plasma boundary resulting from the new representation of λ , the radial current J^s continues to be internally represented (in terms of the full-grid values of λ) on the interlaced grid. This maintains the good radial spatial resolution associated with the original half-grid representation for λ . As a result, computation of accurate, convergent solutions with substantially higher mode numbers is now possible using VMEC2000 (up to poloidal mode numbers $m = 20$). This corresponds to much finer spatial resolution and significantly improved force balance in the final equilibrium state. It also allows the calculation of equilibria with lower values of ι , which were difficult to obtain with the previous differencing scheme.

An additional improvement in the output from VMEC2000 includes an optional recalculation (once the equilibrium has been obtained) of the magnetic force balance $\mathbf{F} \equiv \mathbf{J} \times \mathbf{B} - \nabla p = 0$. The radial (∇_s) component of \mathbf{F} is solved in terms of the nonvanishing contravariant components of B (B^u and B^v) and the metric elements determined by VMEC2000, as a magnetic differential equation for the radial covariant component of the magnetic field, B_s . An angular collocation procedure (with grid points matched to the Nyquist spatial frequency of the modes) is used to avoid aliasing that would arise from the nonlinear mode coupling of the Fourier harmonics of R and Z in the inverse representation of the equilibrium equation. The accurate determination of B_s , together with the higher angular resolution afforded by the larger limits on the allowable m, n spectra in VMEC, permits an accurate assessment for the parallel current (which contains angular derivatives of B_s), as a function of poloidal mode number, to be performed.

III. THE PIES CODE

Three-dimensional magnetic fields in general have magnetic islands and regions of stochastic field lines.

The VMEC code uses a representation of the magnetic field that assumes nested flux surfaces and thus cannot be used to examine magnetic islands. The PIES code is a three-dimensional equilibrium code that uses a general representation for the field and is used for calculating islands and stochastic field line trajectories. There is an extensive set of publications on the algorithm, implementation, validation, convergence properties, and applications of the PIES code.^{3–29}

The PIES code solves the MHD equilibrium equations using a Picard iteration scheme:

$$\nabla \times \mathbf{B}^{(n+1)} = \mathbf{J}(\mathbf{B}^{(n)}) , \quad \nabla \times \mathbf{B}^{(n+1)} = 0 , \quad (1)$$

where the superscripts indicate the iteration number. The iterative steps involve solving for the plasma current \mathbf{J} , given the magnetic field \mathbf{B} and pressure gradient ∇p from the force balance equation,

$$\nabla p = \mathbf{J}^{(n+1)} \times \mathbf{B}^{(n)} , \quad (2)$$

and the constraint

$$\nabla \times \mathbf{J}^{(n+1)} = 0 . \quad (3)$$

This scheme is closely related to the Picard algorithm widely used to solve the axisymmetric Grad-Shafranov equation in the form $\Delta^* \psi_{n+1} = j_\phi(\psi_n)$. As with the Picard iteration scheme for the Grad-Shafranov equation, underrelaxation is used to extend the domain of convergence of the Picard iteration:

$$\mathbf{B}^{(n+1)} = \alpha \mathbf{B}^{(n)} + (1 - \alpha) \mathbf{B} , \quad (4)$$

where $0 < \alpha < 1$, typically $\alpha = 0.98$ or 0.99 for the calculations reported here.

An advantage of solving the equilibrium equations in the form of Eqs. (1), (2), and (3) is that it provides an accurate calculation of resonant pressure-driven currents, which are believed to play an important role in determining island widths. At each iteration, the code solves for the current from the force balance equation. Writing

$$\mathbf{J} = \mu \mathbf{B} + \mathbf{J}_\perp , \quad \mathbf{J}_\perp = \mathbf{B} \times \nabla p / B^2 , \quad (5)$$

gives

$$\mathbf{B} \cdot \nabla \mu = -\nabla \cdot \mathbf{J}_\perp . \quad (6)$$

Integration of this magnetic differential equation gives an accurate method for determining the currents. Gardner and Blackwell³⁰ demonstrated the importance of using an accurate solution for the currents in stability studies, and it is now routine in Mercier and global stability studies of stellarators to recalculate the current from 3-D equilibrium solutions in this way. In implementing a numerical scheme for solving the magnetic differential equation, explicit upper bounds on the associated numerical errors were derived and are used to allow the specification of required tolerances in the code.⁴

As the PIES code iterates, the pressure and current are flattened in islands and stochastic regions. Several numerical diagnostics in the code allow the determination of the locations of these regions. The PIES algorithm is described in detail in the literature.^{3–7,10}

The PIES code has been validated by testing of the individual components, by internal checks in the code that monitor the accuracy with which the equilibrium equations are satisfied, and by comparison with analytic solutions and with other codes. Analytic solutions against which the code has been compared include Soloveev equilibria,⁵ large aspect ratio stellarator expansions,⁵ helical force-free Bessel function equilibria with islands,¹⁰ and analytic solutions for saturated tearing modes with narrow islands. Comparisons of PIES with other codes include axisymmetric j -solver³¹ equilibria for Tokamak Fusion Test Reactor (TFTR) and DIII-D, Biot-Savart vacuum field solvers, marginal stability for tearing modes calculated by linearized resistive time-dependent code, and VMEC (Ref. 8). Reference 8 contains a careful comparison between the VMEC code and the PIES code solutions. The devices modeled were the Advanced Toroidal Facility (ATF) and TJ-II stellarators, for rotational transform profiles where low-order rational surfaces were absent. The flux surface shape, the location of the magnetic axis, and the value of iota as a function of flux surface were monitored as a function of β and radial resolution. An extrapolation in radial resolution was used to verify the quantitative agreement of the codes. The comparison with VMEC was continued in Ref. 9. Here, the rotational transform as a function of radius was in excellent agreement between the two codes for the W7-X stellarator, at $\langle \beta \rangle = 5\%$.

Many stellarators, for example ATF, TJ-II, W7-AS, W7-X, and the Large Helical Device (LHD), have been modeled by the PIES code.^{5,8,9,11}

In the context of the NCSX design effort, several modifications have been made to the PIES code that have increased its speed by about an order of magnitude, allowing routine application of the code to evaluate flux surfaces in candidate NCSX configurations. The speed of the code was improved by modifications to use an improved method for PIES initialization with a VMEC solution, converting to a spline representation of the magnetic field for field line following, and to store matrix inverses. Compared with VMEC, the PIES code has a more time-consuming algorithm, which is needed for a general representation for the magnetic field. Time is saved by initializing PIES with a converged VMEC solution. For this purpose, the underrelaxation scheme in PIES has been modified to provide an improved coupling to the VMEC solution. This involves blending with the VMEC field in the first PIES iteration. The previous underrelaxation scheme blended the current rather than the fields. The underrelaxation was skipped in the first PIES iteration, allowing a large step from the VMEC field but slowing the ultimate convergence. The PIES

code follows magnetic field lines as a preliminary step to solving the magnetic differential equation determining the Pfirsch-Schlueter current. In each iteration of the PIES code, a discretized Ampère's law is solved by the inversion of a block-tridiagonal matrix. The elements of the blocks are determined by metric elements of a "background coordinate system" that does not change from one iteration to the next, allowing time to be saved by storing the inverses of the blocks. For high-resolution calculations, this changes the scaling of the code's execution time from m^3n^3k to a much more favorable m^2n^2k , where m and n are the number of poloidal and toroidal modes retained and k is the number of radial grid surfaces.

IV. FLUX SURFACE INTEGRITY

Three-dimensional magnetic fields in general have magnetic islands and stochastic field lines. In addition, perturbations produced by field errors can break the periodicity of the stellarator and produce additional islands not intrinsic to the equilibrium. Small periodicity-breaking perturbations can be unstable (tearing modes). We do not discuss periodicity-breaking perturbations here, instead focusing on the issue of islands, which are intrinsic to the equilibrium.

The goal in NCSX is to minimize the size of islands and stochastic regions to obtain good flux surfaces across at least 90% of the cross section. As a first step in addressing this issue, a fixed boundary reference configuration with relatively good flux surfaces has been identified,²⁹ and this configuration is referred to as LI383. The intrinsic flux surface properties of configuration LI383 relative to those of other configurations are discussed in this section. Section VI discusses adjustments of the LI383 boundary to remove residual islands. Section VII discusses the design of coils that preserve flux surfaces by suppressing magnetic islands—a procedure called coil healing.

The configuration optimizer used to generate candidate configurations for the NCSX design study did not include a measure of flux surface integrity. Flux surface calculations for the various candidate configurations have found significant differences in the extent of islands and stochastic regions. An earlier reference configuration, referred to as configuration C82, was found to have a large region of stochastic field lines at beta values of interest. This was typical of several types of configurations that were studied. In contrast, the flux surfaces of the NCSX reference design configuration LI383 and similar configurations were nearly adequate even before the application of any flux surface optimization.

In regions where $du/ds > 0$, perturbed bootstrap current effects are predicted to lead to substantially decreased magnetic island widths in configurations of the type studied here.³² This is the inverse of the neoclassical

tearing mode that has been observed in tokamak experiments. This neoclassical effect is presently being incorporated into PIES but is not included in the calculations reported here. The calculations are therefore conservative in that the calculated island widths are likely to be larger than would be observed in an experiment operated in a collisionless regime. Section IX gives an estimate of the neoclassical effect on the island widths.

The PIES calculations discussed in this section are all fixed boundary and used 143 Fourier modes, $0 \leq m \leq 11$ and $-6 \leq n \leq 6$, and 60 radial zones.

Figure 1 shows a Poincaré plot of a fixed-boundary PIES equilibrium for configuration C82 at full current, $\beta = 0$. Magnetic islands occupy about 10% of the cross section. The islands are more readily visible if the Poincaré plot uses a polar (ρ, θ) coordinate system, as in Fig. 2. Here, the coordinate ρ is taken to be constant on VMEC flux surfaces and to measure the distance of the VMEC flux surface from the magnetic axis along the $\theta = 0$, $\phi = 0$ line. The angular coordinate θ is identical to the VMEC angular coordinate. When plotted in these coordinates, the Poincaré plot gives straight lines when the VMEC and PIES solutions coincide.

When β is raised to 3%, the PIES calculations find that a substantial fraction of the flux surfaces is lost (Fig. 3). The equilibrium solution shown is not fully converged. The outer surfaces continue to deteriorate as the calculation progresses, so further computation is of limited interest. From these plots we conclude that flux surface integrity is a problem for configuration C82 in the absence of stabilizing neoclassical effects.

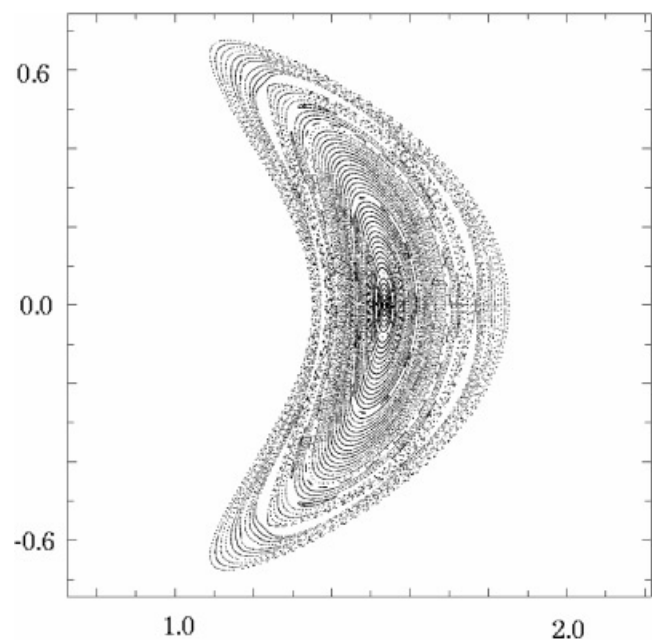


Fig. 1. Poincaré plot for configuration C82 at full current, $\beta = 0$.

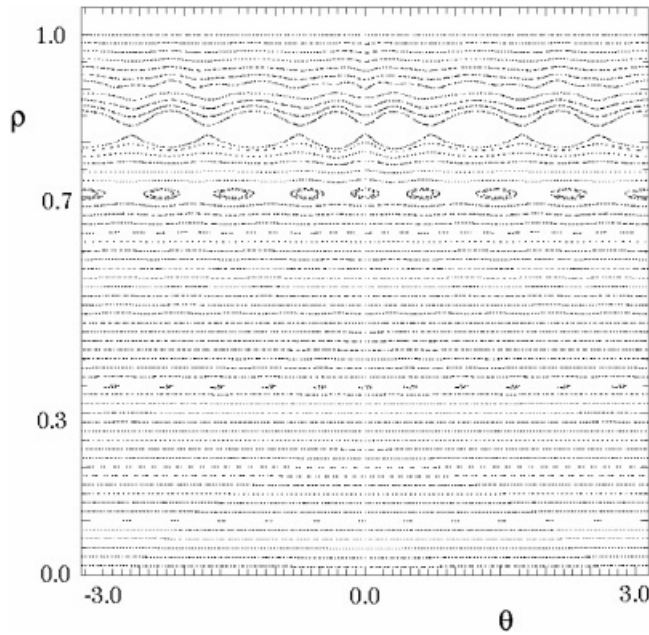


Fig. 2. Poincaré plot for configuration C82 in VMEC coordinates, at full current, $\beta = 0$. The rotational transform ranges from $\iota \approx 0.25$ on axis to $\iota \approx 0.48$ at the edge.

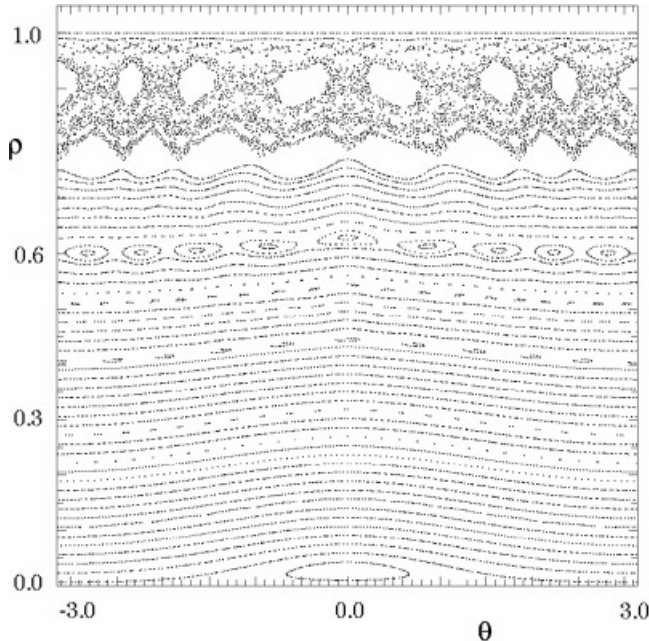


Fig. 3. Poincaré plot for earlier configuration, C82, at full current, $\beta = 3\%$. The rotational transform ranges from $\iota \approx 0.27$ on axis to $\iota \approx 0.46$ at the edge.

Figure 4 shows the result of a PIES calculation for configuration LI383 as originally generated by the optimizer at full current, $\beta = 4.2\%$. The flux surfaces are

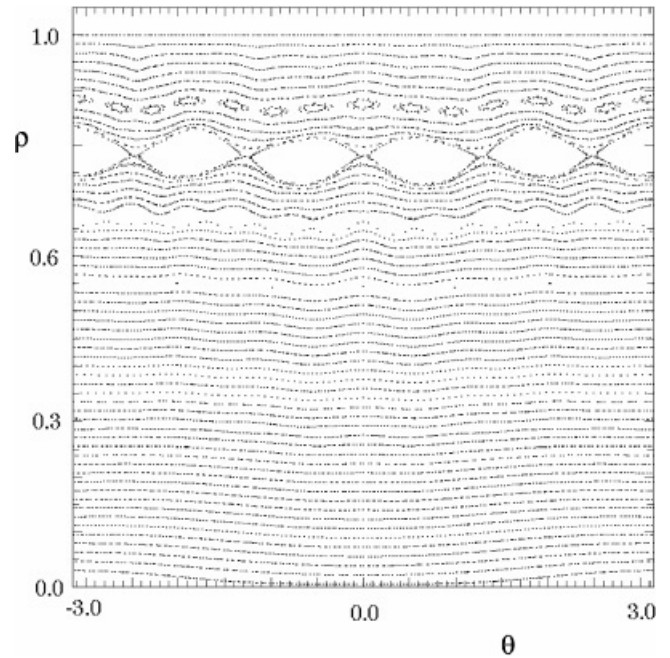


Fig. 4. Poincaré plot for configuration LI383 at full current, $\beta = 4.2\%$.

greatly improved relative to those of configuration C82. The total island width is about 15% and is dominated by a single island chain at $\iota = 0.6$ having poloidal and toroidal mode numbers $m = 5$ and $n = 3$.

The fact that the flux surface loss in the original configuration LI383 is dominated by a single island chain suggests that the flux surfaces can be further improved by adjusting the amplitude of the corresponding resonant Fourier mode in the specification of the boundary shape. This has been demonstrated and is discussed in the following sections.

V. RESONANT FIELDS, ISLANDS, AND QUADRATIC FLUX-MINIMIZING SURFACES

Magnetic islands are caused by resonant radial magnetic fields where the rotational transform is a rational value. The continuous one-dimensional family of periodic orbits that form a rational rotational transform flux surface in the absence of resonant fields will be reduced to a finite set of periodic orbits by the resonant field, and an island chain will form. The periodic orbits surviving perturbation will typically be the stable and unstable periodic orbits, which correspond to the O and X points on Poincaré plots of the magnetic field. In the small island approximation, where the shear ι' is assumed constant across the island, the width of the island is given³³ as $w \propto (|B_{nm}|/\iota'm)^{1/2}$, where $B_{nm} = (\mathbf{B} \cdot \nabla_s / \mathbf{B} \cdot \nabla \phi)_{nm}$ is the resonant Fourier component of the radial field at

the $\iota = n/m$ rational surface, s is the radial coordinate, and the prime represents derivative with respect to s . The phase of the island chain is determined by the sign of B_{nm} and the sign of the shear.

Significant progress in this field of island suppression was made with the introduction of the Cary-Hanson technique,³⁴ which relates the width of magnetic islands to the residue of periodic orbits determined by field line integration, and standard computational optimization routines can be used efficiently to construct coil configurations that produce nested flux surfaces in the vacuum. An alternative technique³⁵ has been applied to the H-1 Heliac.³⁶ Resonant radial fields were determined via construction of quadratic flux-minimizing surfaces, and variations in the vertical field coil currents were used to manipulate the width and phase of magnetic islands in the vacuum field. A configuration was constructed for which vacuum magnetic islands healed as pressure was increased.³⁷

A method for calculating resonant fields at rational surfaces has been incorporated into PIES. This method is based on the construction of quadratic flux-minimizing surfaces.³⁸ The construction of these surfaces has been presented in Ref. 39. The surfaces are defined as extremizing surfaces of the square of the action gradient functional, which is defined as

$$\varphi = \frac{1}{2} \iint [\delta S / \delta \theta]^2 d\theta d\zeta, \quad (7)$$

where the action integral is

$$S = \oint \mathbf{A} \cdot d\mathbf{l}, \quad (8)$$

where

\mathbf{A} = magnetic vector potential

$d\mathbf{l}$ = line segment

\oint = integral along a closed field line.

For the purposes of the present discussion, quadratic flux-minimizing surfaces pass directly through the corresponding island chains and may be considered as rational flux surfaces of an underlying integrable magnetic field.

The construction of the quadratic flux-minimizing surfaces, in essence, provides an optimal magnetic coordinate system, or equivalently an optimal nearby integrable magnetic field, and in these coordinates resonant perturbation harmonics are easily identified. The method is computationally efficient since the quadratic flux-minimizing surfaces defining the coordinate system may be constructed exactly and only where required—at the rational rotational transform surfaces where islands develop. The amplitude of each selected resonant field harmonic is calculated by Fourier decomposing the magnetic field normal to the quadratic flux-minimizing surface. Furthermore, and importantly, the Fourier decomposition is performed using an angle coordinate that corre-

sponds to a straight field line coordinate of the underlying integrable field on that surface.

The rotational transform profile determines which islands will be present in a given configuration, and islands associated with low-order rationals are typically the largest; however, where the shear is small, higher-order islands can easily overlap and result in chaotic field lines and loss of confinement. For the case of LI383, the islands selected for suppression are typically those corresponding to $\iota = 0.5, 0.6$, although higher-order islands are also considered at times. Generally, the lowest-order resonances present will produce the largest magnetic islands. A convenient method of selecting the lowest-order rationals is guided by the Farey Tree construction.⁴⁰

VI. HEALING OF FIXED-BOUNDARY FLUX SURFACES

In this section we consider manipulation of the width and phase of magnetic islands in finite β stellarator equilibria as calculated by PIES by making small variations to the boundary.⁴¹ Magnetic islands are controlled by adjusting the resonant fields at the rational surfaces.

A set of islands that we wish to control is selected. In the case of LI383, clearly the $(n, m) = (3, 5)$ island is dominant. The corresponding set of resonant fields that needs to be controlled is represented by

$$\mathbf{B} = (B_{n_1, m_1}, B_{n_2, m_2}, \dots)^T. \quad (9)$$

We expect that an (n, m) island width will be strongly affected by an (n, m) resonant deformation of the plasma boundary in magnetic coordinates and perhaps through coupling to neighboring modes, so a set of independent boundary variation parameters is constructed as follows. We consider the minor radius,

$$r = \sum r_{nm} \cos(m\theta - nN_p\phi), \quad (10)$$

of the plasma boundary to be a Fourier series in the cylindrical toroidal angle and the poloidal angle used in VMEC to construct the input R and Z harmonics, where N_p is the field periodicity. The conversion to cylindrical space is given as $R = R_0 + r \cos \theta$, $Z = r \sin \theta$. For a change $r \rightarrow r + \delta r_{nm} \cos(m\theta - nN_p\phi)$, the input Fourier harmonics for the VMEC code change according to

$$\begin{aligned} R_{m-1, n} &\rightarrow R_{m-1, n} + \delta r_{nm} / 2, \\ R_{m+1, n} &\rightarrow R_{m+1, n} + \delta r_{nm} / 2, \\ Z_{m-1, n} &\rightarrow R_{m-1, n} - \delta r_{nm} / 2, \\ Z_{m+1, n} &\rightarrow R_{m+1, n} + \delta r_{nm} / 2. \end{aligned} \quad (11)$$

In principle we may change infinitely many boundary harmonics r_{nm} , but a small set is chosen to match the islands targeted, and this becomes the vector of independent parameters

$$\mathbf{r} = (r_{n1m1}, r_{n2m2}, \dots)^T . \quad (12)$$

Now the problem is amenable to standard treatments where the functional dependence of \mathbf{B} on \mathbf{r} is represented:

$$\mathbf{B}(\mathbf{r}_0 + \delta\mathbf{r}) = \mathbf{B}(\mathbf{r}_0) + \mathbf{C} \cdot \delta\mathbf{r} + \dots , \quad (13)$$

where $\mathbf{r}_0 = 0$ is the initial boundary shape and $\delta\mathbf{r}$ is a small boundary variation. The coupling matrix \mathbf{C} represents derivative information and will in general be an $M \times N$ matrix, where M is the number of resonant fields and N is the number of independent boundary variations. The j 'th column of the coupling matrix is determined through a VMEC/PIES run by making a small change $\delta r_{nj, mj}$ and taking the difference in the resonant fields from the original equilibrium, divided by the change. Hence, $N + 1$ VMEC/PIES runs are required to determine the coupling matrix (each PIES run is initialized with a VMEC equilibrium).

The coupling matrix is inverted using the singular value representation,⁴² $\mathbf{C} = \mathbf{U}\mathbf{w}\mathbf{V}^T$, where \mathbf{U} and \mathbf{V} are orthonormal and \mathbf{w} is the diagonal matrix of singular values. If there are more variables than equations, more than one solution may exist, and the nullspace is spanned by the columns of \mathbf{U} corresponding to zero singular values, of which there will be at least $N-M$. Islands are removed if $\mathbf{B} = 0$, so by choosing a correction to the boundary $\delta\mathbf{r}$ according to

$$\delta\mathbf{r}_{i+1} = -\mathbf{V}\mathbf{w}^{-1}\mathbf{U}^T\mathbf{B}_i , \quad (14)$$

where as in standard singular value decomposition techniques the zero, and if desired the small, eigenvalues are ignored in the inversion of \mathbf{w} and \mathbf{B}_i is the vector of resonant fields at the i 'th iteration. In practice, several iterations will be required to achieve a desired accuracy.

This technique was applied to configuration LI383. In Fig. 5 a Poincaré plot of the PIES field after 32 iterations shows island chains, and the $\iota = 3/5$ island is significant. In this figure and in Fig. 6, the Poincaré section is the $\phi = 0$ plane and 50 field lines are followed along the $\theta = 0$ line. In addition, field lines at the X points of several low-order island chains are followed and the quadratic flux-minimizing surface and an estimated separatrix has been plotted over one period of each island chain. The separatrix of the island chains has been calculated using the resonant radial field and the shear at the rational surface of the VMEC equilibrium. PIES has not yet converged for this case, but the information about the island width is still useful for construction of the coupling matrix.

In this application of the island reducing technique, the (3,5), (6,10), (3,6), and (6,12) resonances are targeted, and the (3,9), (3,8), (3,7), (3,6), (3,5), and (3,4) boundary harmonics are varied. The (6,10) resonance produces an island at the same rational surface as the (3,5), namely at $\iota = 3/5$, and may be considered as the second harmonic of the (3,5) resonance. If the (6,10) resonant field is not targeted, this may cause an island of distinct topology from the (3,5). The (3,6) and (3,12) resonances are included to ensure that elimination of the

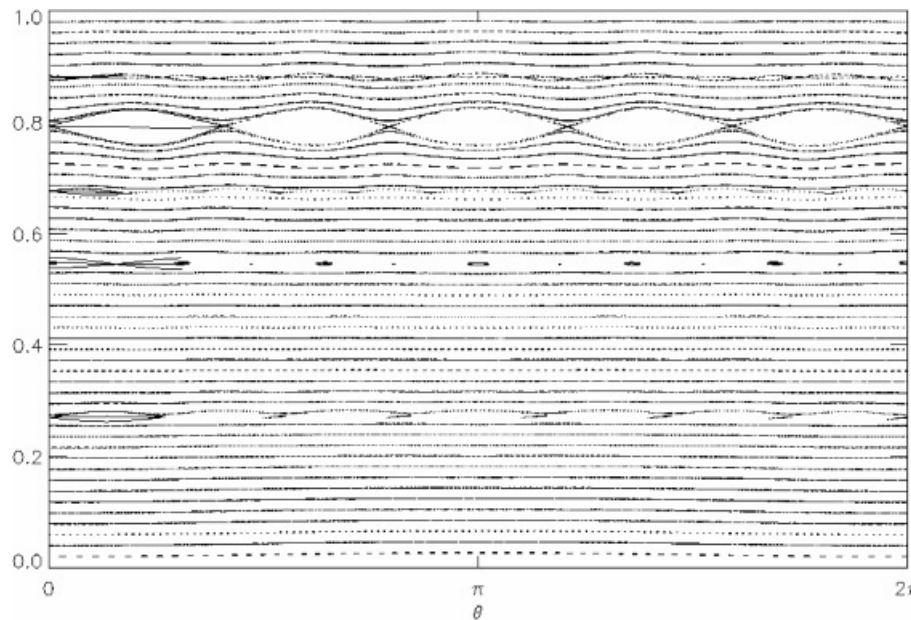


Fig. 5. Poincaré plot of initial LI383 configuration after 32 PIES iterations. For selected island chains, the separatrix and the quadratic flux-minimizing surface (which passes directly through the island chain) has been plotted as the solid line over one period of the island chain.

(3,5) island does not cause a (3,6) island to grow. The (3,7) resonance is also present in the configuration, but this has not been included. For this set of resonant fields and independent boundary variation parameters, the coupling matrix is

$$\begin{pmatrix} \delta B_{3,5} \\ \delta B_{6,10} \\ \delta B_{3,6} \\ \delta B_{6,12} \end{pmatrix} = \begin{pmatrix} -0.15603 & 0.94645 & -0.73397 & -1.13506 & -0.17282 & -0.30578 \\ 0.12627 & 0.17790 & 0.02146 & 0.19875 & -0.07025 & 0.01394 \\ -0.05487 & -0.22773 & -0.50056 & 0.24140 & -0.30079 & 0.01531 \\ -0.00874 & 0.03067 & -0.00351 & 0.00827 & -0.00327 & -0.00083 \end{pmatrix} \begin{pmatrix} \delta_{3,9} \\ \delta_{3,8} \\ \delta_{3,7} \\ \delta_{3,6} \\ \delta_{3,5} \\ \delta_{3,4} \end{pmatrix}.$$

On performing the Newton iterations, the reduction in resonant fields shown in Table I is observed.

The Newton iterations are terminated after four steps since this provides sufficient reduction of the islands, as seen in Fig. 6. In a true Newton iteration procedure, the coupling matrix would be recalculated at every iteration. In this application such a procedure is too slow and the coupling matrix is not changed; nevertheless, the convergence is satisfactory. The total change in the boundary variation parameters is

$$\delta \mathbf{r} = (-0.00184, -0.00026, 0.00056, 0.00300, 0.00012, 0.00064)^T. \quad (15)$$

These variations are several millimeters in magnitude and generally have little impact on stability and other physics. However, the case shown does destabilize the ballooning modes on some surfaces. This would be expected to relax the pressure gradient slightly on those surfaces. This is not surprising considering that the L1383 configuration has been optimized to provide marginal ballooning stability at full pressure.

The healed configuration has converged after 32 iterations, as has been confirmed by an extended PIES run for hundreds of iterations. If the equilibrium has no islands, or if the width of the islands is less than the radial grid used in PIES, then PIES and VMEC will agree and PIES will rapidly converge.

TABLE I

Reduction in Resonant Fields on Performing the Newton Iterations

Iteration	$ B_{3,5} $	$ B_{6,10} $	$ B_{3,6} $	$ B_{6,12} $
0	1.8×10^{-3}	1.6×10^{-4}	1.3×10^{-4}	1.4×10^{-5}
1	1.3×10^{-4}	3.4×10^{-5}	1.0×10^{-4}	2.4×10^{-6}
2	6.7×10^{-5}	3.4×10^{-5}	5.1×10^{-5}	1.9×10^{-6}
3	2.4×10^{-5}	6.7×10^{-5}	4.0×10^{-16}	5.4×10^{-7}

VII. HEALING OF FREE-BOUNDARY FLUX SURFACES: "COIL HEALING"

VII.A. Algorithm for Healing of Free-Boundary Flux Surfaces

The previous two sections have discussed the design of the fixed-boundary configuration to obtain good flux surfaces in equilibria where the shape of the boundary is specified. In the coil design process, a discrete set of coils is produced that targets the desired boundary shape, and the coils are further modified using the merged optimizer to allow for the simultaneous targeting of engineering and physics objectives in the coil design. The result is a plasma that is stable to ideal modes and a coil design that is buildable; however, flux surface quality is not guaranteed by this process, and islands reappear in the free-boundary equilibria.

This section discusses the modification of the coils to heal the flux surfaces while preserving various engineering and physics measures of the free-boundary equilibrium. The method is based on the free-boundary version of the PIES code. Island suppression is achieved by adding to the standard PIES algorithm a procedure that alters the coil geometry *at each iteration* so that selected resonant components of the coil magnetic field cancel the resonant components of the plasma magnetic field—thus eliminating islands. The changes in coil geometry are constrained to preserve both engineering constraints and ideal kink stability. As the iterations continue, the coil geometry and the plasma simultaneously converge to an island-free coil-plasma equilibrium.

An early attempt⁴³ at healing free-boundary PIES equilibria by variation of the coil geometry calculated the resonant fields after a fixed number N_{it} of PIES iterations in which the coil geometry was unchanged. The resonant fields were expressed as a function of coil geometry, and a method essentially identical to the fixed-boundary healing method was used to vary the coil geometry to reduce the resonant fields after N_{it} iterations. This method had some success in healing coil sets; however, the PIES calculations were typically not converged after the fixed

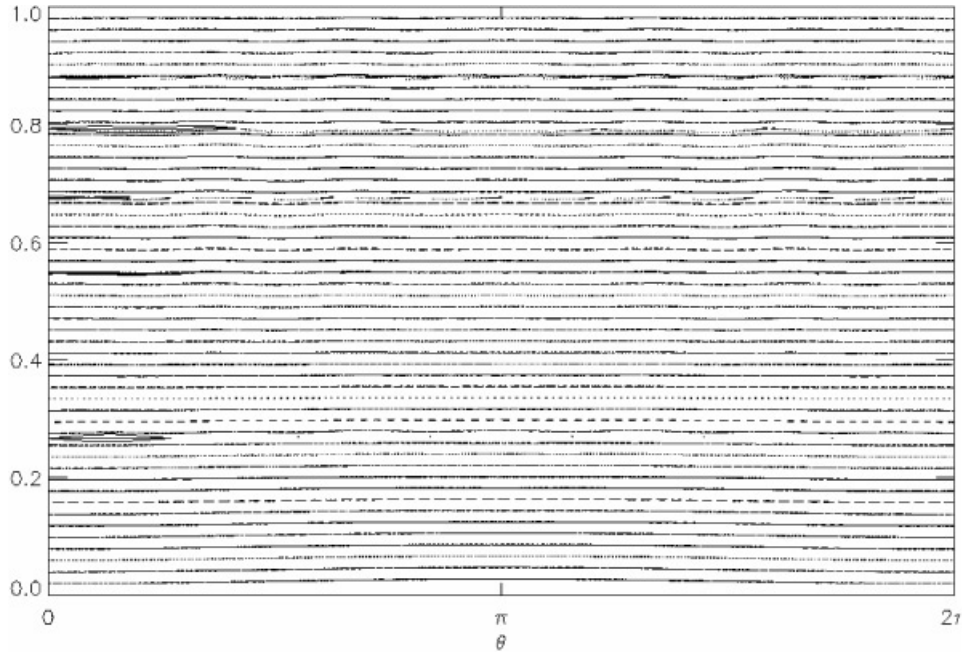


Fig. 6. Poincaré plot of full-beta island-reduced LI383 configuration.

number N_{it} iterations, and there was no guarantee that the configuration would remain healed (this is in contrast to the fixed-boundary healing method, where PIES was initialized by the VMEC equilibrium for each trial boundary, which was not the case here). Experience from this work led to the method presently used to heal free-boundary surfaces—termed dynamic healing—which alters the coil geometry at each PIES iteration and is now described.

The dynamic healing procedure amounts to a free-boundary coil physics optimizer that preserves good flux surfaces, satisfies engineering constraints, and includes measures of physics stability. It is this procedure that leads to healed coil sets, and this procedure is also called coil healing or island healing.

The dynamic healing procedure is obtained by including in the basic PIES the module COILOPT (Ref. 44) and STELLOPT, which are used to alter the coil geometry and evaluate physics measures. Solving the equilibrium equation and the adjustment of a coil design to eliminate selected magnetic islands proceeds with initialization given

$$\mathbf{B} = \mathbf{B}_p^n + \mathbf{B}_C(\xi)^n . \quad (16)$$

The total magnetic field is the sum of the magnetic field produced by the plasma, \mathbf{B}_p , and the magnetic field produced by the confining coils, \mathbf{B}_C , which is a function of a set of Fourier harmonics ξ that describe the coil geometry at the n 'th iteration. The initial plasma state is provided by the VMEC code, which imposes the artificial constraint that the plasma is consistent with nested flux

surfaces. The constraint is generally associated with the appearance of delta function currents at the rational surfaces. The method presented in this section can be considered as removing this constraint and imposing the condition that there be no delta function currents, allowing the VMEC initialization to relax into an equilibrium, potentially with broken flux surfaces (islands), while making adjustments to the coil set to remove selected islands as they develop. The initial coil geometry is provided by the COILOPT code.

As described, the standard PIES algorithm will calculate the plasma current from the field, and then the plasma field from the current. The additional steps in the implementation of the coil healing are as follows. The total magnetic field \mathbf{B} after one PIES iteration is written

$$\mathbf{B} = \mathbf{B}_p^{(n+1)} + \mathbf{B}_C(\xi)^{(n)} . \quad (17)$$

We may consider \mathbf{B} as a small perturbation to a nearby integrable field and that magnetic islands are caused by fields normal to, and resonant with, rational rotational transform flux surfaces of the nearby integrable field. A set of resonances that are to be suppressed is selected, for each resonance a quadratic flux-minimizing surface is constructed, and the set of resonant fields thus calculated is denoted $\{\underline{B}_i; i = 1, N\}$.

The COILOPT code provides a convenient Fourier representation of the coil geometry, and a set of coil harmonics $\{\xi_j; j = 1, M\}$ appropriate for the resonances selected are systematically varied to set $\underline{B}_i = 0$ using a Newton method. The coupling matrix $\nabla \mathbf{B}_{Cij}^n$ is defined as the partial derivatives of the selected resonant harmonics

of the coil magnetic field normal to the quadratic flux-minimizing surface (held constant during each PIES healing iteration) with respect to the chosen coil harmonics and is calculated using finite differences. A multidimensional Newton method is applied to find the coil changes $\delta\xi_j$ that set $B_i = 0$:

$$\underline{B}_i = \nabla \mathbf{B}_{Cij}^n \cdot \delta\xi_j^n . \quad (18)$$

This equation is solved for the $\delta\xi_j$ in a few iterations by inverting the $N \times M$ matrix $\nabla \mathbf{B}_{Cij}^n$ using singular value decomposition and the new coil set is obtained,

$$\xi_j^{(n+1)} = \xi_j^n + \delta\xi_j^n , \quad (19)$$

such that the resonant component of the combined plasma-coil field is eliminated. As the iterations proceed, the coil geometry and the plasma simultaneously converge to coil geometry–plasma solution with good flux surfaces.

The algorithm as presented is insufficient for practical purposes because no consideration has been given to various engineering constraints. To be “buildable,” the minimum coil curvature and coil-coil separation, for example, must exceed certain limits. Such constraints are included in the COILOPT code, and the initialization coil set, described by ξ^0 , is satisfactory from an engineering perspective. The healing algorithm is modified to pre-

serve the minimum curvature and coil-coil separation by adding to the set of resonant fields to be eliminated the (appropriately weighted) differences in minimum curvature and coil separation of the n 'th coil set, described by ξ^n , from the initial coil set. This constrains the island-eliminating coil variations to lie in the nullspace of these measures of engineering acceptability.

In a similar manner, the algorithm is extended to preserve kink stability. The VMEC initialization is stable with respect to kink modes. By calculating kink stability using the TERPSICHORE and VMEC codes, which are executed via the STELLOPT routine, the coil changes are constrained to preserve kink stability.

VII.B. Application of Coil Healing to M45 Coils: Healed Coils M45h

We consider now a coil set referred to as the *M45 coil set*, which was constructed to reproduce the LI383 plasma boundary using the VMEC free-boundary code, so that the issue of flux surfaces was not initially addressed. The $(n, m) = (3, 6), (3, 5)$ islands were selected to be suppressed, subject to the constraint that the minimum coil curvatures, the coil-coil separation, and the kink stability be preserved (nine constraints). For this purpose, some $m = 3, 4, 5, 6, 7, 8$ modular coil harmonics were allowed

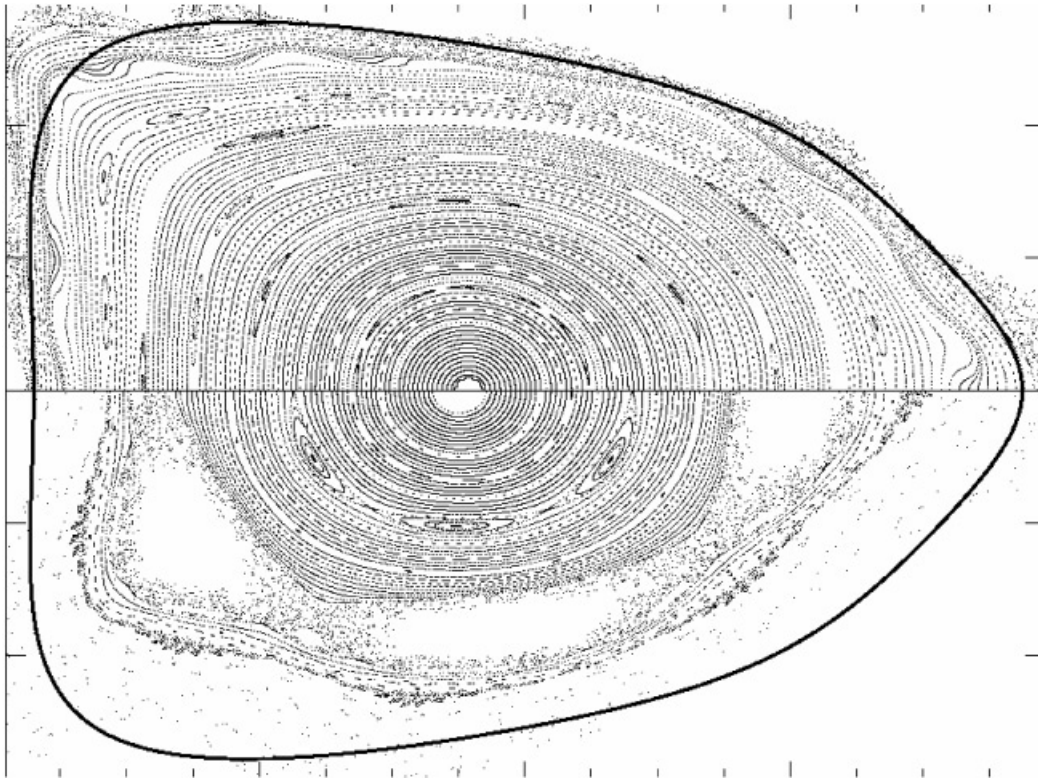


Fig. 7. Poincaré plots before (lower) and after (upper) free-boundary healing of flux surfaces from M45 coils. $\beta = 4.1\%$. The thick solid line corresponds to the plasma boundary in the VMEC solution used to initialize the PIES calculation.

to vary (36 independent variables), and a healed coil-plasma state was achieved. The engineering measures were preserved, with the plasma stable with respect to kink modes. The plasma retains quasi-axisymmetry. About 250 iterations, using a relaxation parameter $\alpha = 0.98$, are required to approach convergence in both the plasma field and the coil geometry. To confirm that the coil set is healed, about 200 additional standard PIES iterations are performed with the coil set unchanged. The coil set obtained is called the *healed M45 coil set* and is renamed *M45h*.

A Poincaré plot of the final field is shown for an up-down symmetric toroidal cross section in the upper half of Fig. 7. The thick solid line in this figure corresponds to the plasma boundary in the VMEC solution used to initialize the PIES calculation. For this calculation and those described below, the pressure profile on the good flux surfaces is held fixed. The VMEC boundary is not treated as a limiter so that the region of nonzero pressure gradient can extend outside that boundary on sufficiently deformed flux surfaces. The island content in the healed configuration is small, though there is some resonant $m = 18$ deformation near the zero shear location (indicating that additional *near*-resonant modes may need suppressing, or that the maximum ι needs to be constrained to avoid the resonance) and some high-order ($m = 10, 11, 12$, and 14) island chains (which are considered sufficiently small). For comparison, a Poincaré plot of the unhealed configuration after 180 standard PIES iterations is shown in the lower half of the figure. For the unhealed case there is a large $m = 5$ island, the edge has become chaotic, and the configuration deteriorates into large regions of chaos as the iterations continue.

A broad selection of coil harmonics was varied since the coil harmonics are not decomposed in a magnetic angle and thus cannot be expected to couple directly with the resonant field harmonics of the plasma. Also, by doing so there is extra freedom that is utilized by the singular value decomposition method to find a solution with minimal coil change. The coil harmonics varied actually describe the toroidal variation of the modular coils on a topologically toroidal winding surface. The winding surface itself is described using a Fourier representation, but the winding surface is not altered in this procedure. The calculation shown used 63 radial surfaces and 12 poloidal and 6 toroidal modes. Similar results have been obtained using up to 93 radial surfaces and 20 poloidal modes.

The maximum coil alteration is about 2 cm, which comfortably exceeds manufacturing tolerances but is not so large that “healing” significantly impacts other design concerns, such as diagnostic access. A plot of the original coils and the healed coils in VMEC toroidal coordinates is shown in Fig. 8. From this figure we can see that the healed coils, from an engineering perspective, are essentially the same as the original coils; in particular, the coil-coil separation and minimum coil bend radius are the same for the M45h coils and the original M45 coils.

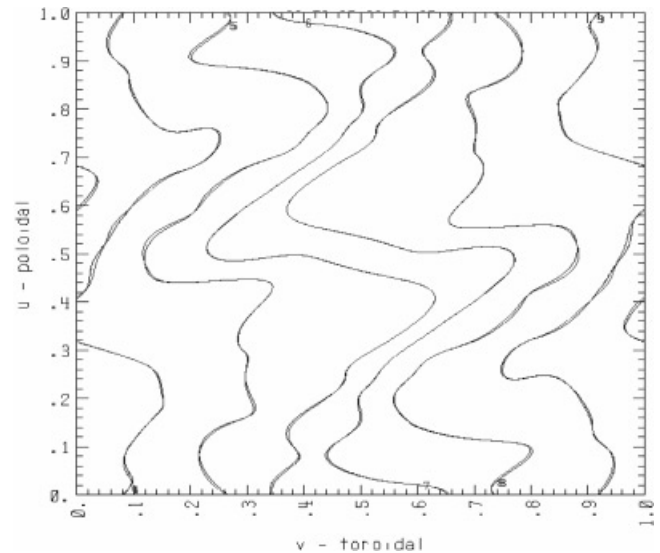


Fig. 8. Original M45 coils and healed M45h coils in U - V space.

VIII. MAGNETIC FIELDS PRODUCED BY THE HEALED COILS

VIII.A. Finite Thickness Healed Coil Set

The analysis of coil sets thus far has used single filament coil representations. The single filament model simply positions a filament at the geometrical center of each coil along the winding path. Because the difference between the healed and unhealed coils is about 2 cm, it is required to confirm that the finite thickness of the coils to be built will not adversely affect the quality of the flux surfaces. A finite model coil configuration, based on the healed coil set, is obtained as follows. The modular coils are modeled as rectangles in cross section, 0.12 m in height and 0.10 m in width, with a 0.02-m web at the center that separates each coil into two halves. There are 8 by 2 turns for each coil half, and each turn is modeled as a filament. This coil model resembles the proposed winding discussed in the engineering design document.

We first note that the multifilament coil model preserves the quasi-axisymmetry for the healed coils, M45h. Using effective ripple as a measure of quasi-symmetry, the results of a NEO transport calculation based on VMEC equilibria show that the difference is less than 1.5% between single- and multifilament models throughout the entire plasma volume. The effective ripple is 0.21% at $r/a = 0.5$ for the single-filament model, whereas it is 0.213% for the multifilament model. Similarly, at $r/a = 0.9$ it is 1.026% for the single-filament versus 1.029% for the multifilament model. Also, the multifilament coils are stable with respect to kink and ballooning modes.

PIES calculations indicate that the flux surfaces are similar in quality for both single- and multifilament

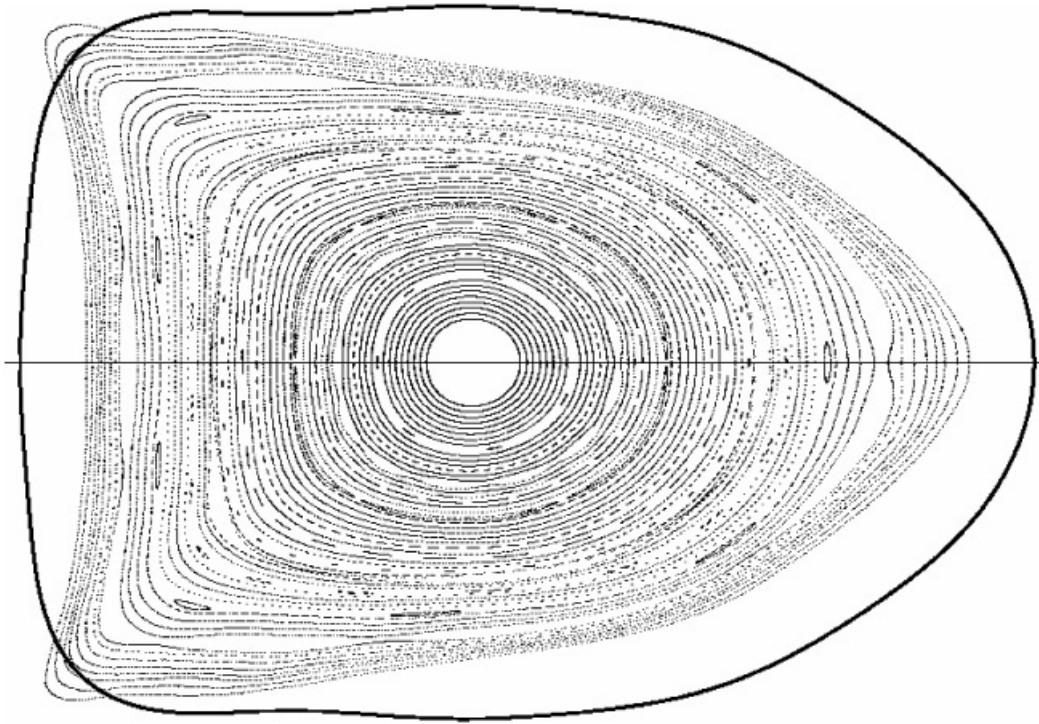


Fig. 9. PIES equilibrium using the multifilament healed coils (M45h) at $\beta = 4.1\%$. The first wall boundary is shown as the thick solid line. This figure compares favorably to single-filament equilibrium in Fig. 7.

models of the healed coils (M45h) at the reference operating state. Using the multifilament coil set constructed, a PIES run was performed and the converged equilibrium is shown in Fig. 9. The flux surface quality of the equilibrium actually appears to be better than that in the single-filament coil case. The area of greatest improvement is the absence of the resonant $m = 18$ deformation near the zero shear region.

Figure 9 displays several good surfaces that extend beyond the first wall boundary. That is not an issue for these surfaces because they lie in the vacuum region, outside the surface where the imposed pressure profile goes to zero.

The improvement in flux surface quality in going from single-filament to multifilament coil representations suggests that the remaining Poincaré plots, which are all single-filament calculations, may be conservative and that the finite coil build may improve flux surface quality for these configurations.

VIII.B. Vacuum Configurations with the Healed Coils

The coil healing procedure considered only the full-pressure and full-current configuration; nevertheless, the healed coils produce plasma states at different pressure and current with good flux surfaces over most of the plasma volume. This section will present an analysis of a variety of vacuum states.

Various vacuum configurations are shown that confirm that good flux surfaces may be obtained with the healed coils (M45h) for a number of cases. The different rotational transform profiles, varying from 0.43 to 0.46, 0.52 to 0.53, 0.52 to 0.54, 0.54 to 0.56, and 0.54 to 0.58, are shown in Fig. 10. The corresponding Poincaré plots are shown in Figs. 11 through 15. The adjustment of the rotational transform in the vacuum is achieved by variation of the coil currents. These plots all show good flux surfaces, to varying degrees, and indicate that a variety of starting points may be used to generate plasma evolution sequences that will ultimately reach the healed, operating configuration. In all of these plots the location of the first wall is shown as the thick solid line.

VIII.C. Comparison of Healed Coils and Unhealed Coils at an Alternative Configuration

The coils have been modified to heal the islands in the reference configuration. We find that, having reduced the amplitude of the resonant magnetic field components produced by the coils in this configuration, the flux surfaces are improved in other configurations as well. This is illustrated by Fig. 16, which shows the results of PIES calculations using the healed and unhealed coils for a configuration that arises in a start-up scenario. The PIES calculations have been done for a time slice at 303 ms, with a β of 4.6%, and the configuration is stable to

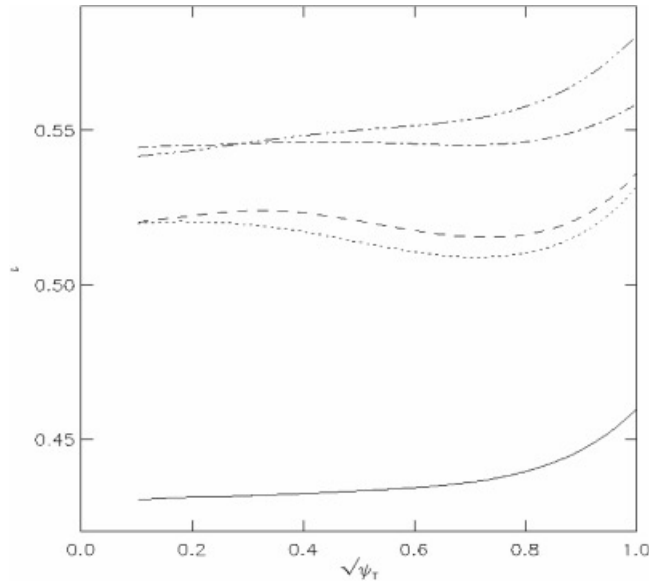


Fig. 10. Rotational transform profiles corresponding to vacuum cases shown in Figs. 11 through 15.

ballooning and kink modes. The upper half of the Poincaré plot is for the healed coils, and the bottom half for the unhealed coils. The flux surface quality of the healed coils for this configuration is far better than that of the unhealed coils. The PIES run for the unhealed coils is not converged and continues to deteriorate as the calculation proceeds.

This plot shows that the healed coils (M45h) produce improved flux surface quality in a configuration other than the configuration for which the healing was performed.

The improvement of flux surface quality in going from a single-filament coil model to a multifilament model and the fact that the healed coils display better flux surface quality than the unhealed coils in a variety of configurations suggest that the healing process has provided a distinctly improved set of coils for the NCSX experiment.

IX. NEOCLASSICAL HEALING OF MAGNETIC ISLANDS

IX.A. Introduction

The purpose of this section is to estimate the effect of the neoclassical bootstrap current in reducing the width of magnetic islands in a “reversed shear” quasi-axisymmetric stellarator such as NCSX. It has been recognized for some time³² that the bootstrap current, which can destabilize “neoclassical tearing modes” in tokamaks, is stabilizing in a stellarator with outwardly increasing transform, i.e., positive dv/dr . There is experimental evidence for the neoclassical stabilizing effect

from the LHD stellarator.^{45,46} The magnitude of this effect depends on plasma collisionality, both through the dependence of the bootstrap current on the parameter ν_{*e} and through the role of finite parallel thermal conduction in limiting temperature flattening across the island.

In the present analysis, we employ the formalism of tokamak theory: The only stellarator-specific effect is an externally imposed chain of magnetic islands with mode numbers corresponding to the dominant nonsymmetric field “perturbation” in the NCSX configuration. For simplicity, we neglect two other effects, namely resonant Pfirsch-Schlüter currents and stabilizing resistive-interchange contributions, which are expected to be less important than the bootstrap current effect in the cases considered here. Note that in considering the effects of the bootstrap current, we do not modify the global current profile but only assume that some fraction of it is driven by the bootstrap effect. That fraction of the current will then go to zero inside the islands when the pressure gradient is flattened there, producing a helical modification of the current that gives rise to the neoclassical effect.

IX.B. Bootstrap Current Effect on Magnetic Islands

For cylindrical tokamak geometry, including the bootstrap current density j_{bs} , the island width w in the weakly nonlinear regime^{47–49} grows according to

$$(\mu_0/1.2\eta) dw/dt = \Delta' + 6.4(\mu_0 L_q/B_\theta) j_{bs}/w, \quad (20)$$

where Δ' is the usual tearing-mode stability quantity and $L_q = q/q'$. The numerical coefficient 6.4 arises from calculating the applicable Fourier component of the current perturbation caused by zeroing the bootstrap current inside the magnetic island, i.e., within the area bounded by the island separatrix.⁵⁰ Writing

$$j_{bs} = -C_{bs}(\varepsilon^{0.5}/B_\theta) dp_e/dr, \quad (21)$$

where $\varepsilon = r/R$ and C_{bs} is a numerical coefficient of order unity that describes the dependences of the bootstrap current on the density and temperature profiles and on the collisionality parameter ν_{*e} , we obtain

$$(\mu_0/1.2\eta) dw/dt = \Delta' + 3.2C_{bs}\varepsilon^{0.5}\beta_{\theta e}(L_q/L_{pe})/w, \quad (22)$$

where $L_{pe} = -p_e/p_e'$. For the tokamak ($q' > 0$), the bootstrap current term is positive and can overcome a negative Δ' to produce unstable neoclassical tearing modes. Comparisons with experimental data from tokamaks have generally suggested a numerical coefficient somewhat smaller than 3.2 in this equation; for example, analysis of neoclassical tearing modes in TFTR gave a coefficient of 2.6 (Ref. 51). For present purposes, however, we will retain the somewhat larger theoretical coefficient.

The case of an island produced by the vacuum magnetic fields in a quasi-axisymmetric stellarator may be

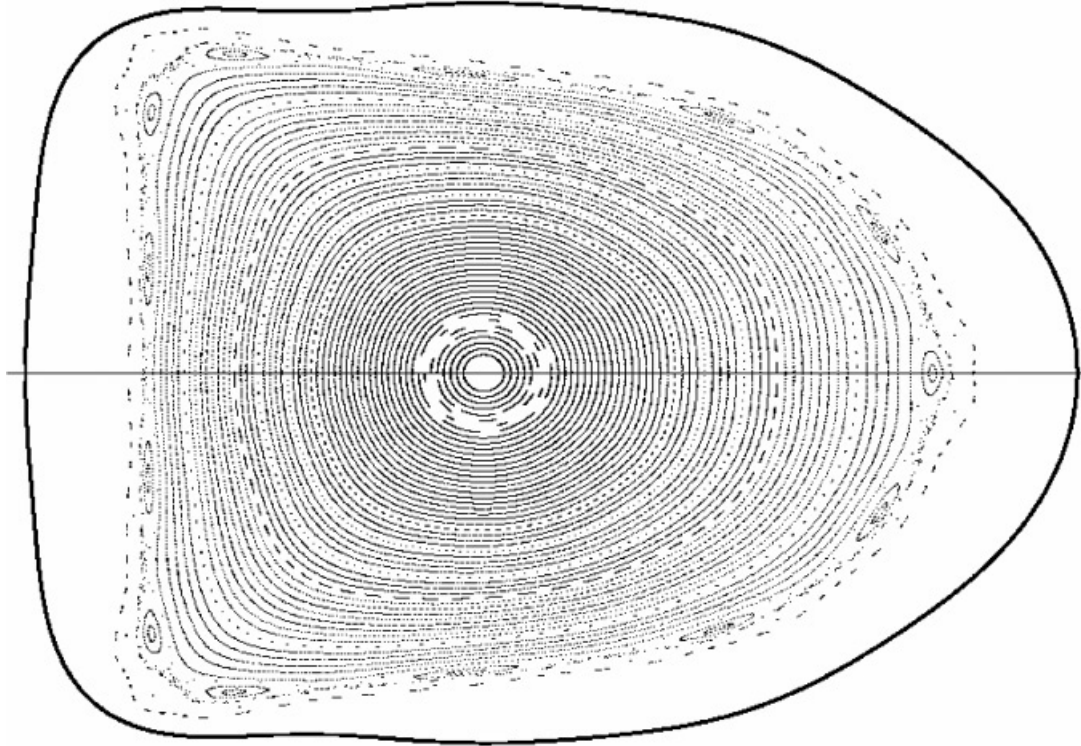


Fig. 11. Vacuum configuration, $\iota = 0.43$ to 0.46 , with healed coils (M45h). The first wall boundary is shown as the thick solid line.

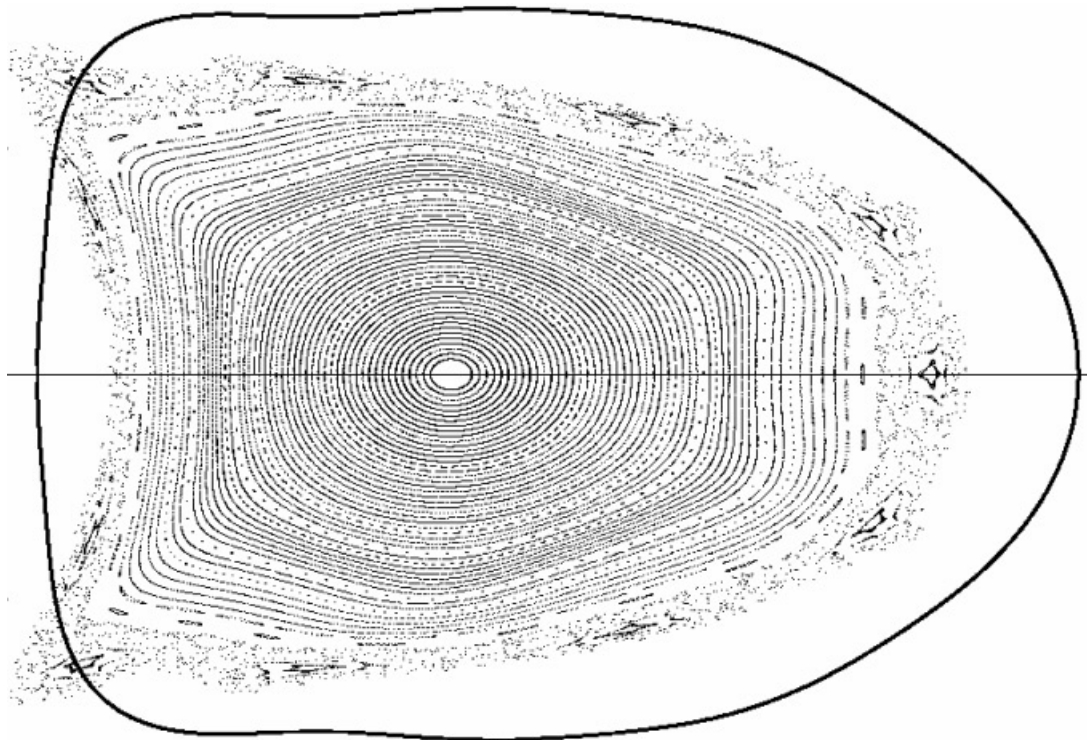


Fig. 12. Vacuum configuration, $\iota = 0.52$ to 0.53 , with healed coils (M45h). The first wall boundary is shown as the thick solid line.

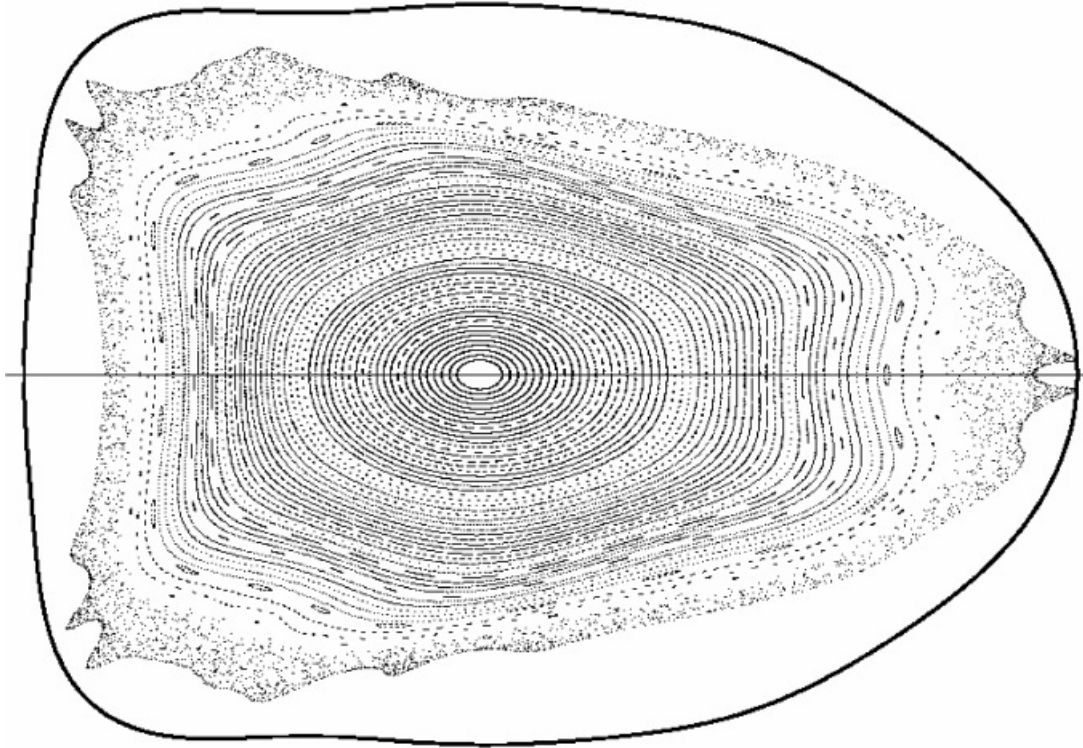


Fig. 13. Vacuum configuration, $\iota = 0.52$ to 0.54 , with healed coils (M45h). The first wall boundary is shown as the thick solid line.

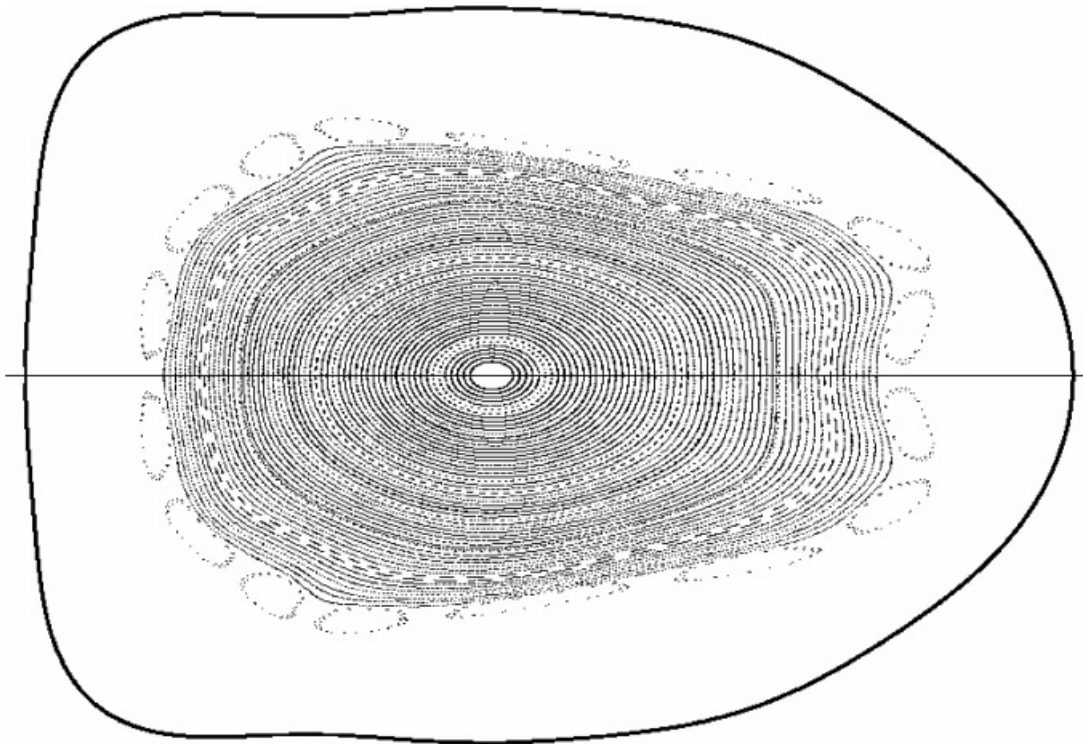


Fig. 14. Vacuum configuration, $\iota = 0.54$ to 0.56 , with healed coils (M45h). The first wall boundary is shown as the thick solid line.

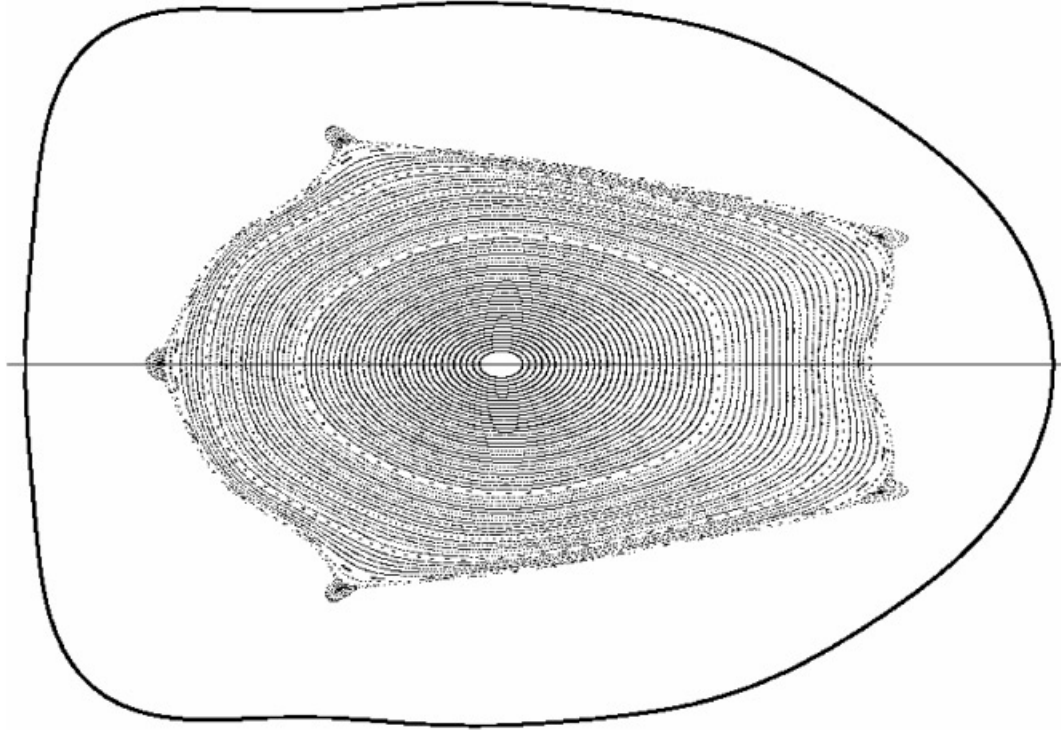


Fig. 15. Vacuum configuration, $\iota = 0.54$ to 0.56 , with healed coils (M45h). The first wall boundary is shown as the thick solid line.

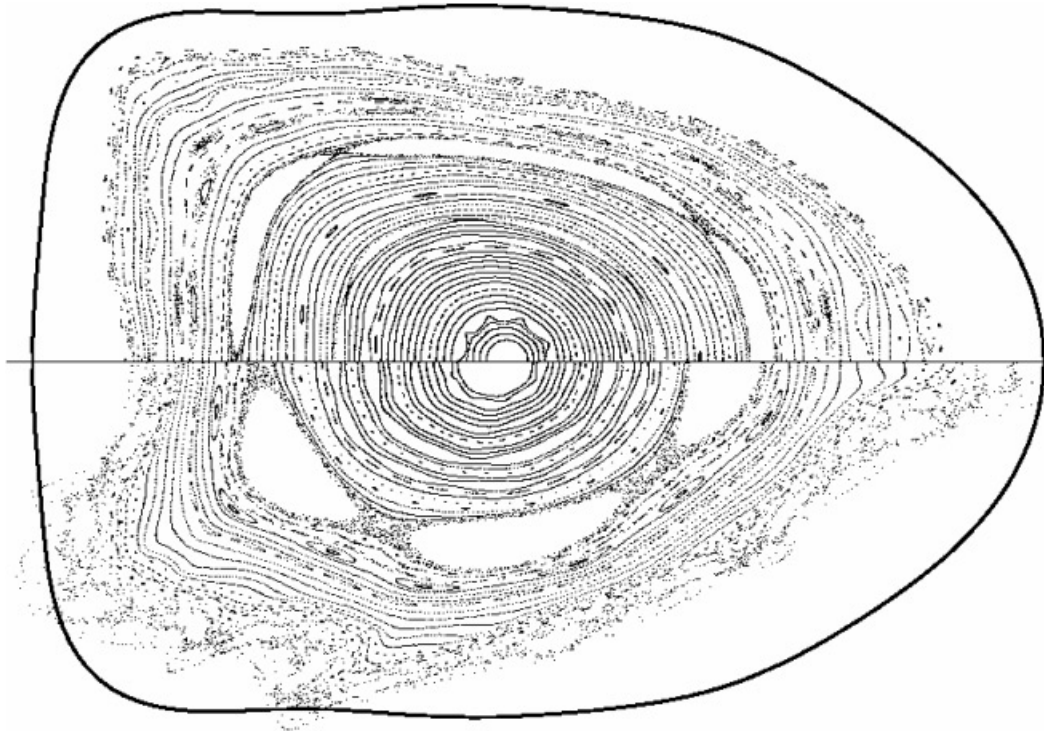


Fig. 16. Start-up evolution sequence time 303 ms at $\beta = 4.6\%$. The upper half is with the healed coils (M45h), and the lower half is with the unhealed coils (M45). The healed coils show significant improvement. The first wall boundary is shown as the thick solid line.

considered analogous to the case of a tokamak in which an island is produced by superimposing an external helical magnetic perturbation that is resonant on a magnetic surface within the plasma. If such a perturbation were imposed dynamically, then the plasma would respond initially (i.e., within ideal MHD theory) by forming a helical sheet current on the resonant surface. This sheet current would then decay resistively, producing a magnetic island; when the width of this island exceeds the very narrow resistive layer of linear tearing-mode theory, it will be described by an appropriate generalization of the slow-growing tearing-mode theory. In the present context, we are interested in the case where the resonant helical perturbation has mode numbers m and n for which the tearing mode would be stable, i.e., for which Δ' is negative. (Accordingly, we henceforth write $\Delta' = -|\Delta'|$.)

It is straightforward to extend the theory of weakly nonlinear tearing modes³² to include an externally driven island. Rather than introducing the external perturbation explicitly, it is more convenient simply to describe it in terms of the island width w_{ext} that would be produced after resistive relaxation of the currents on the scale length of the island but *without* the bootstrap current effects. Adding the bootstrap current term as before, the island is found to evolve according to

$$(\mu_0/1.2\eta) dw/dt = -|\Delta'| (1 - w_{ext}^2/w^2) - 3.2C_{bs} \varepsilon^{0.5} \beta_{\theta e} (L_i/L_{pe})/w . \quad (23)$$

Here we have also written $L_q = -L_i = -\iota'/\iota$ in order to use the quantity $\iota = 1/q$ that is more appropriate to a stellarator and to indicate that in this case the bootstrap term is stabilizing. For a high- m mode, to a very good approximation, we may use

$$\Delta' = -2m/r . \quad (24)$$

The “skin time” for resistive relaxation of w toward w_{ext} without bootstrap effects may now be estimated, namely $\tau_s = (\mu_0/1.2\eta)(2w_{ext}r/m)$.

The bootstrap current term is seen to be inversely proportional to the island width w . This arises from the implicit assumption that density and temperature gradients are completely flattened across the magnetic island, thereby zeroing the bootstrap current within the island. Since electron thermal conduction is by far the fastest process of equilibration along field lines in high-temperature plasmas, bootstrap current drive (or healing) of magnetic islands arises most effectively from the flattening of the electron temperature gradient, with flattening of the density gradient being less effective. Since in most practical cases (including the cases considered here) the electron temperature gradient provides the dominant contribution to the bootstrap current anyway, because the density profile is relatively flat, it is not unreasonable to employ the full bootstrap current in calculations such as

these, but it should be recognized that this may give an overestimate of the bootstrap current effect on magnetic islands in some cases.

For very narrow islands, however, the path length along the helical field lines becomes very long, and finite (as distinct from effectively infinite) electron thermal conduction along the field lines will prevent the electron temperature from flattening fully across the island, thereby reducing even the most effective process of bootstrap current island drive or healing. This effect is introduced into the theory⁵⁰ by modifying the bootstrap current term as follows:

$$1/w \Rightarrow w/(w^2 + w_0^2) , \quad (25)$$

where we have defined a “critical island width” w_0 , namely

$$w_0 = 5.1(\chi_{\perp}/\chi_{\parallel})^{0.25} (RL_i/m\iota)^{0.5} . \quad (26)$$

Here, χ_{\perp} and χ_{\parallel} are the perpendicular and parallel thermal diffusivities, which control the degree to which the temperature is flattened across the island.

Setting $dw/dt = 0$, we then find the following relation to describe the actual island width w in terms of w_{ext} with bootstrap current effects included:

$$w_{ext}^2/w^2 = 1 + 2w_{bs}w/(w^2 + w_0^2) , \quad (27)$$

where we have introduced an island width characterizing the bootstrap current effect, namely

$$w_{bs} = 1.6C_{bs} \varepsilon^{0.5} \beta_{\theta e} (L_i/L_{pe})/|\Delta'| . \quad (28)$$

IX.C. Assumed NCSX Parameters and Profiles

We have assumed the following parameters for the reference NCSX high-beta plasma:

$$R = 1.4 \text{ m} ,$$

$$a = 0.32 \text{ m (average)} ,$$

$$\langle \beta \rangle = 4.2\% ,$$

$$B_0 = 1.2 \text{ T} ,$$

and

$$\langle n_e \rangle = 5.8 \times 10^{19} \text{ m}^{-3} . \quad (29)$$

We have used density and temperature profiles that correspond very closely to those resulting from transport calculations for NCSX (Ref. 52), namely,

$$n_e(r) = 7.8(1 - r^2/a^2)^{0.35} (10^{19} \text{ m}^{-3}) ,$$

$$T_e(r) = 2.8(1 - r^2/a^2)^{1.35} (\text{keV}) ,$$

and

$$T_i(r) = 1.9(1 - r^2/a^2)^{0.75} (\text{keV}) . \quad (30)$$

The use of profiles that are parabolas raised to exponents α_n and α_T facilitates the calculation of the bootstrap current from the relevant theory. We have used an iota profile for the reference configuration for which the iota = 0.6 surface falls at $r/a = 0.8$. The only other quantity needed from the iota profile is the local shear length, which for this profile is given by $L_\iota/a = 0.7$. It should be noted that the shear length L_ι may be longer for iota profiles that flatten or decrease toward the plasma edge.

IX.D. Bootstrap Current Magnitude

To evaluate the bootstrap current term, i.e., the characteristic island width w_{bs} , it is essential to have a good estimate for the constant C_{bs} , since this can vary appreciably depending on profiles and on plasma collisionality. For present purposes, we have assumed the profiles given above and have employed the Hinton-Rosenbluth neoclassical theory for the “banana/plateau transition,”⁵³ taking $Z_{eff} = 1.5$. We have allowed for $T_i \neq T_e$ and have included both the ∇T_e and ∇T_i contributions to the bootstrap current. We obtain collisionality parameters (at the resonant surface $r/a = 0.8$) given by $\nu_{*e} = 0.49$ and $\nu_{*i} = 0.27$. For the profiles assumed and for these collisionality parameters, we then obtain $C_{bs} = 1.37$, which gives

$$w_{bs}/a = 0.28 . \quad (31)$$

In practical units, the value of C_{bs} found here corresponds to a bootstrap current density at the resonant surface $r/a = 0.8$ given by $j_{bs} = 60$ A/cm². This value is close to the peak of the bootstrap current density profile in this case, because of the strong local pressure gradient and modest collisionality in the region of the resonant surface. This value agrees reasonably well with other calculations of the bootstrap current density in the NCSX reference configuration.

For the case considered here, the major contribution to the bootstrap current arises from the electron temperature gradient. This is partly because the density gradient is relatively small and partly because the coefficient in the transport matrix that multiplies the electron temperature gradient falls off less strongly with collisionality than does the coefficient multiplying the density gradient. The ion temperature gradient is found to make only a small contribution to the bootstrap current.

IX.E. Critical Island Width w_0

To evaluate the critical island width w_0 , we need estimates for the perpendicular and parallel electron thermal diffusivities. We obtain an estimate for χ_\perp from its relation to the energy confinement time τ_E . Using $\tau_E \approx a^2/4\chi_\perp$ together with the empirically projected energy confinement time in NCSX of 25 ms, we obtain an estimate $\chi_\perp \approx 1.0$ m²/s.

Obtaining a good estimate for χ_\parallel is trickier. We start by calculating the Spitzer parallel electron thermal diffusivity at the resonant surface; this gives $\chi_\parallel^{Sp} \approx 2.9 \times 10^9$ m²/s. If we use this value in the expression for w_0 , we would obtain $w_0/a \approx 0.02$. However, at low collisionality, the electron mean free path typically exceeds the parallel wavelength along the helical perturbations. In such cases, the use of Spitzer thermal diffusivity may lead to unphysically large parallel heat fluxes, and thermal diffusion must effectively be replaced by thermal convection, according to the relationship $\chi_\parallel \nabla_\parallel^2 T_e \Rightarrow v_{the} \nabla_\parallel T_e$, where v_{the} is the electron thermal velocity. The quantity ∇_\parallel is the inverse parallel wavelength along the helical perturbation, which depends on the island width w and can be estimated as $\nabla_\parallel \approx (mw/R) dv/dr = mw/RL_\iota$. Since χ_\parallel appears only to the one-quarter power, it is not necessary to retain this explicit dependence on the island width w and so, for present purposes, we simply estimate it as $w/a \approx 0.05$. For the “effective” thermal diffusivity in this convection-limited regime, we obtain $\chi_\parallel^{eff} \approx 7.2 \times 10^7$ m²/s. If we use this value in the expression for w_0 , we would obtain $w_0/a \approx 0.05$ (validating our estimate used to obtain χ_\parallel^{eff}).

Without more theoretical work, it is not obvious which value to use for w_0 . Almost certainly, the Spitzer thermal diffusivity will overestimate parallel heat transport at low collisionality. On the other hand, fast electrons may still be able to equilibrate the temperature at a rate faster than that given by convection at the thermal speed. Accordingly, it might be appropriate to take a range $w_0/a = 0.03$ to 0.04 . In the calculation of the bootstrap island effect given below, we have simply chosen an intermediate value, namely

$$w_0/a \approx 0.035 . \quad (32)$$

It has been pointed out⁵⁴ that islands of widths less than w_0 would not be expected to have a seriously deleterious effect on confinement because transport from one side of the island to the other along the direct path is already larger than transport along the path that follows the helical field lines. For the high- β NCSX reference case, this effect would apply only to islands with widths less than about 1 cm. However, the effect (unlike the bootstrap current) does not depend on the plasma beta value, and it increases strongly with higher collisionality, so it should apply particularly to low-temperature preheated plasmas. The Spitzer parallel thermal diffusivity scales as $T_e^{2.5}$, so a reduction in the temperature at the resonance surface to 100 eV (from 700 eV in the high- β plasma) would result in an increase in w_0/a to about 0.08. (Since parallel thermal convection scales much more weakly with electron temperature than thermal diffusivity, we find that the Spitzer diffusivity would be the operative process in this case.) This result suggests that in low-temperature ohmic plasmas in NCSX, islands at the iota = 0.6 surface as large as about 2.5 cm may not have a seriously detrimental effect on confinement.

TABLE II

Neoclassical Bootstrap-Healed Island Widths w for Various Externally Generated Island Widths w_{ext} at the $\iota = 0.6$ Surface in the Reference NCSX High- β Configuration

w_{ext} (cm)	w (cm)
1.0	0.41
2.0	0.70
3.0	1.00
4.0	1.34
5.0	1.73
6.0	2.19

IX.F. Results for NCSX Reference Case

The actual island widths w for a range of possible “externally produced” island widths w_{ext} are given in Table II. For this calculation, we have taken $w_{bs}/a = 0.28$ and a value $w_0/a = 0.035$ (see the preceding discussions). For external islands with widths in the range 2 to 6 cm (i.e., 6 to 18% of the minor radius), the bootstrap current reduces the island width by almost a factor of 3.

IX.G. Conclusions Concerning Neoclassical Healing

The depletion of bootstrap current within the island causes a substantial reduction in the width of the magnetic island caused by the dominant nonsymmetric field “perturbation” in NCSX. Specifically, for the 4% beta reference NCSX configuration, the bootstrap current should reduce the width of the $m/n = 5/3$ islands at the $\iota = 0.6$ surface by almost a factor of 3.

The bootstrap current in NCSX is sufficient for this purpose despite the relatively high collisionality of the plasma, which puts the island region (where $\nu_{*e} \approx 0.5$) in the “banana plateau transition,” rather than “pure banana,” regime of neoclassical transport. For the cases considered, the main contribution to the bootstrap current comes from the electron temperature gradient, rather than the density gradient. The key element in ensuring sufficient bootstrap current is a relatively high value of the local $\beta_{\theta e}$ at the resonant surface together with a relatively steep local electron pressure gradient.

X. CONCLUSIONS

The calculation of 3-D equilibria for stability and transport assessments of candidate NCSX configurations has been performed with the VMEC code. This code makes the simplifying assumption that nested magnetic flux surfaces exist, which greatly increases the speed of the calculation. To calculate the 3-D equilibria with is-

lands and stochastic regions, the PIES code is used, which relaxes the assumption of nested flux surfaces at the cost of computational speed. Critical improvements have been made to both VMEC and PIES during the course of the NCSX design.

The PIES code has been used to improve the flux surface quality of the reference configuration by guiding the introduction of small modifications to the configuration that reduce the resonant magnetic field components. In fixed-boundary equilibria, the island content is reduced by alteration of the boundary, and in free-boundary equilibria, the island content is reduced by variation of the coil geometry.

The latter technique, termed coil healing, in essence amounts to a free-boundary stellarator plasma-coil design algorithm, which adjusts the coil geometry to obtain a plasma equilibrium with selected islands suppressed while simultaneously preserving certain engineering constraints and stability measures. This method was used to obtain the healed reference coil set M45h referred to throughout this paper.

The flux surface quality of plasma configurations generated by the healed coil set M45h have been extensively studied. Using a multifilament coil description to model the finite build of the coils, the PIES calculation shows that the flux surface quality is improved relative to that of the single-filament healed coils. Vacuum states with various rotational transform profiles are shown that confirm that the healed coils allow good flux surfaces in the vacuum. Also, a comparison of the healed coils with the unhealed coils for an alternative high- β configuration from the start-up modeling shows that the healed coils produce improved flux surface quality, relative to the unhealed coils, for configurations for which the coils were not optimized. Having reduced the amplitude of the resonant magnetic field components produced by the coils in the reference configuration, the flux surfaces are improved in other configurations as well.

Finally, neoclassical and $\chi_{\perp}/\chi_{\parallel}$ effects are estimated. Neoclassical effects are predicted to produce a substantial reduction in the island widths relative to those calculated by the PIES code. The effect of finite $\chi_{\perp}/\chi_{\parallel}$ is to give a threshold island width $w_0 \approx 0.035a$, below which islands have little impact on confinement.

Including the corrections due to the finite neoclassical and $\chi_{\perp}/\chi_{\parallel}$ effects, an assessment of the flux surfaces as calculated by PIES for a range of configurations, including the reference configuration with single- and multifilament coils, five different vacuum configurations, and five equilibria representing snapshots at different times in a start-up scenario, indicate that the flux surfaces for the healed coil set M45h are acceptable.

ACKNOWLEDGMENT

This work has been supported by U.S. Department of Energy contract DE-AC02-76CH03073.

REFERENCES

1. S. P. HIRSHMAN and D. K. LEE, *Comput. Phys. Commun.*, **39**, 161 (1986).
2. S. P. HIRSHMAN, W. I. VAN RIJ, and P. MERKEL, *Comput. Phys. Commun.*, **43**, 143 (1986).
3. A. REIMAN and H. S. GREENSIDE, *Comput. Phys. Commun.*, **43**, 157 (1986).
4. A. REIMAN and H. S. GREENSIDE, *J. Comput. Phys.*, **75**, 423 (1988).
5. H. GREENSIDE, A. REIMAN, and A. SALAS, *J. Comput. Phys.*, **81**, 102 (1989).
6. A. REIMAN and N. J. POMPHREY, *Comput. Phys.*, **941**, 225 (1991).
7. D. A. MONTICELLO, P. MERKEL, J. L. JOHNSON, and A. H. REIMAN, *Proc. 10th Int. Conf. Stellarators*, Madrid, Spain, May 22–26, 1995 (1995).
8. J. L. JOHNSON, D. A. MONTICELLO, A. H. REIMAN, A. SALAS, A. L. FRAGUAS, and S. P. HIRSHMAN, *Comput. Phys. Commun.*, **77**, 1 (1993).
9. P. MERKEL, J. L. JOHNSON, D. A. MONTICELLO, et al., *Proc. 14th Int. Conf. Plasma Physics and Controlled Nuclear Fusion Research*, Würzburg, Germany, September 30–October 7, 1992, Paper IAEA-CN-60/D-P-II-10, International Atomic Energy Agency, Vienna, Austria (1994).
10. A. H. REIMAN and H. S. GREENSIDE, *J. Comput. Phys.*, **87**, 349 (1990).
11. J. L. JOHNSON, D. A. MONTICELLO, and A. H. REIMAN, *Proc. 15th Int. Conf. Numerical Simulations of Plasmas*, King of Prussia, Pennsylvania (1994).
12. A. H. REIMAN and D. MONTICELLO, *Phys. Fluids B*, **3**, 2230 (Aug. 1991).
13. A. H. REIMAN and D. MONTICELLO, *Nucl. Fusion*, **32**, 1341 (1992).
14. R. J. GOLDSTON, G. H. NEILSON, D. B. BATCHELOR, et al., *Fusion Technol.*, **21**, 1039 (May 1992).
15. A. LOPEZ FRAGUAS, A. SALAS, A. H. REIMAN, D. A. MONTICELLO, and J. L. JOHNSON, *Proc. Ninth Kiev Int. Conf. Plasma Theory*, Kiev, Ukraine, July 1992, p. I-577 (1992).
16. S. C. JARDIN, A. BHATTACHARJEE, A. BONDESON, et al., *Proc. 14th Int. Conf. on Plasma Physics and Controlled Nuclear Fusion Research*, Würzburg, Germany, September 30–October 7, 1992, Paper IAEA-CN-56/D-4-13, International Atomic Energy Agency, Vienna, Austria (1992).
17. D. A. MONTICELLO, A. H. REIMAN, and C. Y. WANG, *Proc. Ninth Int. Workshop on Stellarators*, Garching, Germany, May 10–14, 1993, p. 114, International Atomic Energy Agency, Vienna, Austria (1993).
18. A. SALAS, A. LOPEZ FRAGUAS, A. H. REIMAN, D. A. MONTICELLO, and J. L. JOHNSON, *Proc. Ninth Int. Workshop on Stellarators*, Garching, Germany, May 10–14, 1993, p. 127, International Atomic Energy Agency, Vienna, Austria (1993).
19. P. MERKEL, J. L. JOHNSON, D. A. MONTICELLO, and A. H. REIMAN, *Proc. Ninth Int. Workshop on Stellarators*, Garching, Germany, May 10–14, 1993, p. 133, International Atomic Energy Agency, Vienna, Austria (1993).
20. J. L. JOHNSON, D. A. MONTICELLO, A. H. REIMAN, and C. WANG, *Proc. Ninth Int. Workshop on Stellarators*, Garching, Germany, May 10–14, 1993, p. 121, International Atomic Energy Agency, Vienna, Austria (1993).
21. J. A. SCHMIDT, K. I. THOMASSEN, R. J. GOLDSTON, et al., *J. Fusion Energy*, **12**, 221 (1993).
22. J. NUHRENBURG, P. MERKEL, C. SCHWAB, et al., *Plasma Phys. Control. Fusion*, **35** Suppl., B115 (Dec. 1993).
23. J. MANICKAM, M. S. CHANCE, S. C. JARDIN, et al., *Phys. Plasmas*, **1**, 1601 (1994).
24. P. MERKEL, J. L. JOHNSON, D. A. MONTICELLO, A. H. REIMAN, A. SALAS, and A. L. FRAGUAS, *Proc. 15th Int. Conf. Plasma Physics and Controlled Nuclear Fusion Research*, Seville, Spain, September 1994, International Atomic Energy Agency, Vienna, Austria (1994).
25. D. A. MONTICELLO, J. L. JOHNSON, A. H. REIMAN, and P. MERKEL, *Proc. 10th Int. Workshop on Stellarators*, Madrid, Spain, May 22–26, 1995, EUR-CIEMAT 30, p. 45 (1995).
26. R. J. LaHAYE et al., *Proc. 16th IAEA Fusion Energy Conf.*, Montreal, Canada, October 7–11, 1996, Paper F1-CN-64/AP1-21, International Atomic Energy Agency, Vienna, Austria (1996).
27. A. REIMAN, L. P. KU, D. MONTICELLO, C. NUEHRENBURG, and W. COOPER, *Plasma Phys. Reports*, **23** 472 (1997).
28. S. ARNDT, P. MERKEL, D. A. MONTICELLO, and A. H. REIMAN, *Phys. Plasmas*, **6**, 1246 (1999).
29. A. REIMAN, L. KU, D. MONTICELLO, et al., *Phys. Plasmas*, **8**, 2083 (2001).
30. H. GARDNER and B. BLACKWELL, *Nucl. Fusion*, **33** (1993).
31. J. DELUCIA, S. C. JARDIN, and A. M. M. TODD, *J. Comput. Phys.*, **37**, 183 (1980).
32. C. C. HEGNA and J. D. CALLEN, *Phys. Plasmas*, **1**, 3135 (1994).
33. A. J. LICHTENBERG and M. A. LIEBERMAN, *Regular and Chaotic Dynamics*, 2nd ed., Springer-Verlag, New York (1992).
34. J. D. HANSON and J. R. CARY, *Phys. Fluids*, **27**, 767 (1984).

35. S. R. HUDSON and R. L. DEWAR, *Phys. Lett. A*, **226**, 85 (1997).
36. M. G. SHATS, D. L. RUDAKOV, B. D. BLACKWELL, L. E. SHARP, R. TUMLOS, S. M. HAMBERGER, and O. I. FEDYANIN, *Nucl. Fusion*, **34**, 1653 (1994).
37. S. S. LLOYD, H. J. GARDNER, T. HAYASHI, and S. R. HUDSON, *J. Plasma Fusion Res.*, **1**, 484 (1997).
38. R. L. DEWAR, S. R. HUDSON, and P. PRICE, *Phys. Lett. A*, **194**, 49 (1994).
39. S. R. HUDSON and R. L. DEWAR, "Analysis of Perturbed Magnetic Fields via Construction of Nearby Integrable Field," *Phys. Plasmas*, **6**, 5, 1532 (1999).
40. J. D. MEISS, "Symplectic Maps, Variational Principles and Transport," *Rev. Modern Phys.*, **64**, 3, 362 (1992).
41. S. R. HUDSON, D. A. MONTICELLO, and A. H. REIMAN, *Phys. Plasmas*, **8**, 7, 3377 (2001).
42. W. H. PRESS, B. P. FLANNERY, S. A. TEUKOLSKY, and W. T. VETTERLING, *Numerical Recipes in Fortran 77: The Art of Scientific Computing*, Cambridge University Press, Cambridge, U.K.
43. S. R. HUDSON, A. REIMAN, D. STRICKLER, A. BROOKS, D. A. MONTICELLO, and S. P. HIRSHMAN, *Plasma Phys. Control. Fusion*, **44**, 7, 1377 (2002).
44. D. J. STRICKLER, L. A. BERRY, and S. P. HIRSHMAN, "Designing Coils for Compact Stellarators," *Fusion Sci. Technol.*, **41**, 2, 107 (2002).
45. K. NARIHARA, K. Y. WATANABE, I. YAMADA, et al., *Phys. Rev. Lett.*, **87**, 135002-1 (2001).
46. N. OHYABU, K. IDA, T. MORISAKI, et al., *Phys. Rev. Lett.*, **88**, 055005-1 (2002).
47. P. H. RUTHERFORD, *Phys. Fluids*, **16**, 1903 (1973).
48. J. D. CALLEN et al., *Proc. 11th Int. Conf. Plasma Physics and Controlled Nuclear Fusion Research*, Kyoto, Japan, Vol. 2, p. 157, International Atomic Energy Agency, Vienna, Austria (1987).
49. C. C. HEGNA, J. D. CALLEN, T. A. GIANAKON, et al., *Plasma Phys. Control. Fusion*, **35**, 987 (1993).
50. R. FITZPATRICK, *Phys. Plasmas*, **2**, 825 (1995).
51. Z. CHANG, J. D. CALLEN, E. D. FREDRICKSON, et al., *Phys. Rev. Lett.*, **74**, 4663 (1995).
52. D. R. MIKKELSON, Personal Communication (Jan. 2001).
53. F. L. HINTON and M. N. ROSENBLUTH, *Phys. Fluids*, **16**, 836 (1973).
54. R. J. GOLDSTON, Personal Communication (June 2000).